Acta Crystallographica Section B
Structural Science
ISSN 0108-7681

Large, larger, largest – a family of cluster-based tantalum copper aluminides with giant unit cells. I. Structure solution and refinement

Thomas Weber,[a] Julia Dshemuchadse,[a] Miroslav Kobas,[b] Matthias Conrad,[c] Bernd Harbrecht[c] and Walter Steurer[a]*

[a]Laboratory of Crystallography, ETH Zurich, Wolfgang-Pauli-Strasse 10, 8093 Zurich, Switzerland, [b]Dectris Ltd, Neuenhoferstrasse 107, 5400 Baden, Switzerland, and [c]FB Chemie, Philipps Universität, 35032 Marburg, Germany

Correspondence e-mail: steurer@mat.ethz.ch

Received 25 February 2009
Accepted 14 April 2009

This is the first of two parts, where we report the structure determination of a novel family of cluster-based intermetallic phases of unprecedented complexity: $cF444$-$Al_{63.6}Ta_{36.4}$ (ACT-19), a = 19.1663 (1) Å, V = 7040 Å^3, $cF(5928 - x)$-$Al_{56.6}Cu_{3.9}Ta_{39.5}$, x = 20 (ACT-45), a = 45.376 (1) Å, V = 93 428 Å^3 and $cF(23\,256 - x)$-$Al_{55.4}Cu_{5.4}Ta_{39.1}$, x = 122 (ACT-71), a = 71.490 (4) Å, V = 365 372 Å^3. The space group is $F\bar{4}3m$ in all three cases. These cluster-based structures are closely related to the class of Frank–Kasper phases. It is remarkable that all three structures show the same average structure that resembles the cubic Laves phase.

1. Introduction

This is the first of two papers discussing the structures of a novel family of intermetallic phases in the system Al–Cu–Ta (part II: Conrad *et al.*, 2009). The interest in cluster-based intermetallics with giant unit cells results from their potentially interesting properties caused by different length scales. These are, on the one hand, the diameters and chemical compositions of the different clusters and, on the other hand, the periodicity and composition of the structure as a whole. Furthermore, some cluster-based intermetallics may have the potential to serve either as a template for the self-organized growth of complex nanoscale structures or even as an ordered analogue to an arrangement of nanoparticles in a matrix.

Prominent examples of cluster-based intermetallics are Zintl phases, metallic clathrates, many Frank–Kasper phases as well as quasicrystals and their approximants. The number of atoms per unit cell ranges from a few tens up to a few thousand. The famous Samson phases $cF1168$-Mg_2Al_3 (Feuerbacher *et al.*, 2007) and $cF1192$-$NaCd_2$ (Fredrickson *et al.*, 2007) belong to the largest ones. The intermetallic phase with the largest number of atoms per unit cell known so far is $mC7448$-$Cu_{4.5}Yb$.[1] It is not (multiple-shell) cluster-based but can be described as a monoclinically distorted $7 \times 7 \times 6.5$ superstructure of the $cF24$-$AuBe_5$ structure type (Černý *et al.*, 1996).

The only ternary compounds in the system Al–Cu–Ta published so far are the Laves phase $hP12$-$Ta(Al_{1-x}Cu_x)_2$, x = 0.14–0.57, which is of the hexagonal $hP12$-$MgZn_2$ type, and the μ phase $hR13$-$Ta_6(Al,Cu)_7$ ($hR13$-W_6Fe_7 type; Nowotny & Österreicher, 1964). Remarkably, working with only Debye–Scherrer diffractograms, the authors noted the probable existence of an additional unknown polyhedral phase in this system, which could have been ACT-45 or ACT-71. $Ta(Al,Cu)_2$ is one of the few true ternary Laves phases, *i.e.* one that is not just the extension of a binary Laves phase. In such cases the hexagonal variant has always been observed (Stein *et al.*,

[1] The Pearson symbol $mC7448$ means *m*onoclinic side *c*entred with 7448 atoms per unit cell.

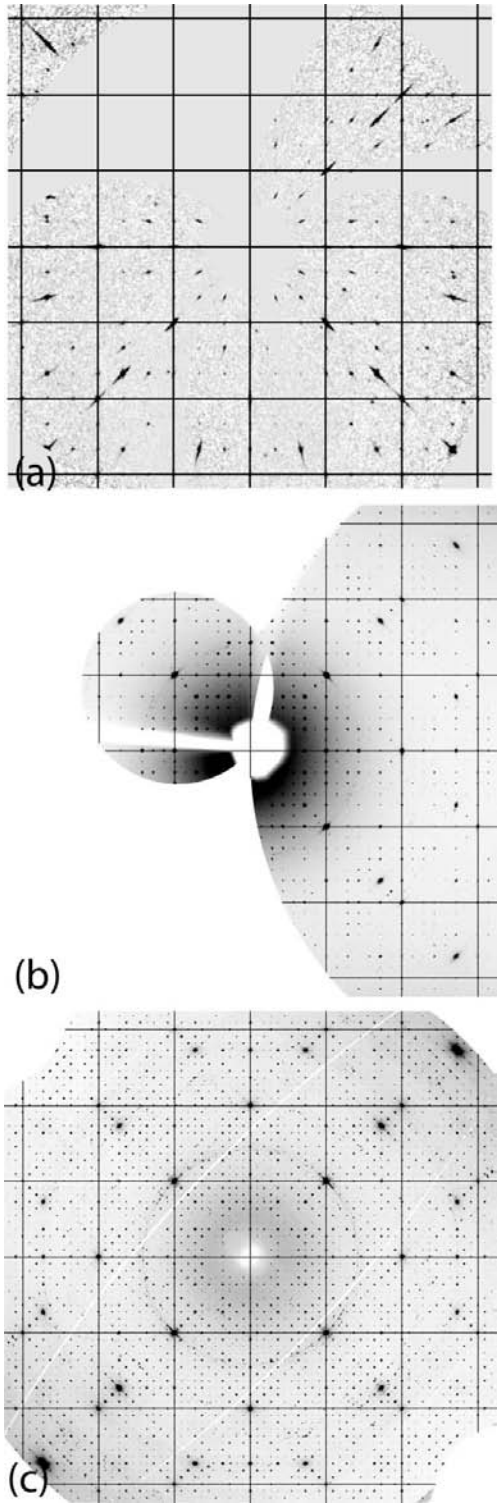

Figure 1
Reciprocal space section of the *hk*0 layers of (*a*) AT-19, (*b*) ACT-45 and (*c*) ACT-71. The maximum extent from the origins along horizontal and vertical directions is 1 Å^{-1} in all cases. The reciprocal lattice of the ∼ 6.5 Å average structure is superimposed on all sections (because the average structure is *F*-centred only grid lines fulfilling the condition $h, k = 2n$, n = integer, are shown). The pattern of ACT-71 was convoluted with a two-dimensional Gaussian with a full width at half maximum (FWHM) of 0.00125 Å^{-1} to avoid the reflections becoming too narrow to be clearly visible (experimental half-width of the Bragg peaks ∼ 0.0007 Å^{-1}). The narrow white arcs in the diffraction pattern of ACT-71 originate from the blind regions of the PILATUS 6M detector.

2005). For Laves phases AB_2, the ideal atomic size ratio amounts to $r_A/r_B = 1.225$. Experimentally observed ratios have been between 1.05 and 1.70 (Stein *et al.*, 2004). In our case the ratios are $r_{Ta}/r_{Cu} = 1.12$ and $r_{Ta}/r_{Al} = 1.0$ ($r_{Al} = 1.432$ Å, $r_{Cu} = 1.278$ Å, $r_{Ta} = 1.430$ Å); however, electropositive atoms appear smaller in an environment of more electronegative atoms. Consequently, the addition of Cu to $TaAl_2$ increases the electronegativity difference and improves the atomic size ratio (Allred and Rochow electronegativity: $\chi_{Al} = 1.5$, $\chi_{Cu} = 1.8$, $\chi_{Ta} = 1.3$).

2. Experimental

2.1. Sample preparation

Crystals of AT-19 were obtained by heating an alloy of composition $Al_{60}Ta_{40}$ above the melting temperature to 2073 K, and then cooling it down to a final annealing temperature of 1773 K at a rate of 100 K h^{-1}. The master alloy was synthesized following the procedure given by Conrad & Harbrecht (2007). AT-19 is a high-temperature phase, stable within the temperature range from 1456 to 1821 K.

Samples containing ACT-71 were first obtained by arc-melting compacts of the elements Al (3N5, < 150 µm), Cu (3N, < 60 µm), Ta (3N, < 45 µm), in the ratio $Al_{55}Cu_5Ta_{40}$ under purified argon (4N8). Since mass loss due to vaporization of Al and Cu cannot easily be controlled under these conditions, further samples were prepared in corundum crucibles in Mo containers, which were sealed gas-tight for reactions at approximately 1873 K. To avoid oxidation as far as possible, the Mo crucibles were outgassed at 2173 K ($P < 10^{-4}$ Pa) before they were sealed. For thermal treatment we used either a self-made, inductively heated, water-cooled double-wall quartz-glass reactor (HFQR) attached to a Himmel HF generator (12 kW) or a high-temperature, high-vacuum furnace (LHTW 60–80/20, Gero). A master alloy of composition $Al_{56}Cu_4Ta_{40}$ was synthesized from compacts of Al/$CuAl_2$/Ta in a HFQR at 1473 K, 15 h. The mass loss was less than 0.1%. A sample with nominal composition $CuAl_2$ was prepared from the elements in the same way at 1473 K (HFQR).

Crystals of ACT-45 were found as a minor component in one sample subsequently heated above the melting temperature to 1893 K, and then cooled down to 1833 K at a rate of 5 K h^{-1}. Mass loss at this temperature was 1.3%. According to energy-dispersive X-ray diffraction (EDX; seven datapoints) the sample had an average composition of $Al_{53.4}Cu_{6.3}Ta_{40.3}$.

Single crystals of ACT-71 were obtained by starting at 1973 K and cooling at a rate of 10 K h^{-1}. An almost-single-phase microcrystalline sample (> 97%) was prepared by annealing a master alloy of composition $Al_{55}Cu_5Ta_{40}$ (1473 K, 24 h). The major competitor of both phases is a previously unknown hexagonal phase, *hP*386, forming at a marginally smaller Cu content and melting congruently at 1863 (5) K according to differential thermal analysis (DTA; setsys 1750, Setaram).

Table 1
Experimental table.

	AT-19	ACT-45	ACT-71
Crystal data			
Chemical formula	$Al_{282.23}Ta_{161.77}$	$Al_{3339.80}Cu_{231.95}Ta_{2336}$	$Al_{12827.56}Cu_{1244.05}Ta_{9063}$
M_r	36 886.85	527 545.12	2 065 084.38
Cell setting, space group	Cubic, $F\bar{4}3m$	Cubic, $F\bar{4}3m$	Cubic, $F\bar{4}3m$
Temperature (K)	293	293	293
a (Å)	19.16630 (10)	45.3760 (10)	71.490 (4)
V (Å^3)	7040.68 (6)	93 428 (4)	365 372 (35)
Z	1	1	1
Radiation type	Mo $K\alpha$	Synchrotron	Synchrotron
μ (mm^{-1})	63.41	70.11	70.04
Crystal form, size (mm)	Irregular, 0.04 × 0.02 × 0.02	Irregular, 0.03 × 0.02 × 0.02	Irregular, 0.01 × 0.005 × 0.005 for I, and 0.02 × 0.03 × 0.04 for II
Data collection			
Diffractometer	Goniometer Xcalibur, detector: Onyx CCD	MAR345 image plate	PILATUS 6M pixel detector
Data collection method	ω scan	φ scans	φ scans
Absorption correction	Multi-scan†	Multi-scan†	Multi-scan†
T_{min}	0.186	0.273	0.54 (for I), 0.17 (for II)
T_{max}	0.364	0.419	0.72 (for I), 0.33 (for II)
No. of measured, independent and observed reflections	33 911, 5264, 3661	157 953, 12 010, 11 816	1 759 829, 48 023, 47 991
Criterion for observed reflections	$I > 2\sigma(I)$	$I > 2\sigma(I)$	$I > 2\sigma(I)$
R_{int}	0.056	0.057	0.042
θ_{max} (°)	67.3	28.8	30.4
Refinement			
Refinement on	F^2	F^2	F^2
$R[F^2 > 2\sigma(F^2)]$, $wR(F^2)$, S	0.038, 0.084, 0.90	0.019, 0.046, 1.08	0.024, 0.061, 1.12
No. of reflections	5264	12 010	48 023
No. of parameters	62	520	1393
$(\Delta/\sigma)_{max}$	0.002	0.003	0.042
$\Delta\rho_{max}$, $\Delta\rho_{min}$ (e Å^{-3})	9.80, −10.35	4.34, −2.79	6.77, −4.38
Absolute structure	Flack (1983), 2374 Friedel pairs	Flack (1983), 5798 Friedel pairs	Flack (1983), 23 408 Friedel pairs
Flack parameter	0.548 (17)	0.376 (5)	0.499 (6)

Computer programs used: *CrysAlis CCD* and *RED* (Oxford Diffraction, 2008), *XDS* (Kabsch, 1993), *SUPERFLIP* (Palatinus & Chapuis, 2007), *SHELXL97* (Sheldrick, 2008). † Based on symmetry-related measurements.

2.2. X-ray experiments, data reduction and observations

2.2.1. AT-19. The X-ray experiment was performed with an Oxford Diffraction diffractometer equipped with an Onyx CCD detector, a Mo X-ray tube and a graphite monochromator adjusted to select the $K\alpha$ lines. The aim of the experiment was to collect a Bragg dataset up to very high angles to have a reliable basis for an accurate determination of atomic occupancies (split atoms) and displacements. The first structure analysis on this compound (Mahne & Harbrecht, 1994) gave partially occupied positions, which should be scrutinized in the light of our quantum-mechanical calculations. The experimental time required for obtaining significant intensities up to our target resolution of 0.4 Å was 180 h. Data were processed with the software *CrysAlis RED* (Oxford Diffraction, 2008). All further experimental details are listed in Table 1.[2]

The reconstructed reciprocal space images exhibit Laue symmetry $m\bar{3}m$ (Fig. 1*a*). The extinction rules are consistent with the space group symmetry $F\bar{4}3m$ reported by Mahne & Harbrecht (1994). The distribution of strong reflections indicates an underlying basic periodicity (average structure) of 6.38 Å, *i.e.* 1/3 × 1/3 × 1/3 of the unit cell. However, since the diffraction pattern cannot be separated into a set of strong main reflections and weak satellites, it cannot be simply described as a commensurately modulated structure. There is no significant diffuse scattering that could be distinguished from the background.

2.2.2. ACT-45. X-ray diffraction data were collected on a MAR345 image-plate system at the Swiss–Norwegian beamline SNBL@ESRF, Grenoble, France. The experiment was done in constant dose mode, *i.e.* the exposure time of individual frames was dynamically adjusted to compensate for primary intensity variations due to refill or decay of the synchrotron storage ring current. Data were collected in two runs on the same crystal. In the first run, the crystal was exposed to a high dose in order to measure weak reflections (174 frames, oscillation angle per frame $\Delta\varphi = 0.5°$, average exposure time ~ 40 s per frame). The primary dose of the second run was reduced by a factor of ~ 40 for measuring the reflections saturated in the first run (285 frames, $\Delta\varphi = 0.5°$,

[2] Supplementary data for this paper are available from the IUCr electronic archives (Reference: SN5082). Services for accessing these data are described at the back of the journal.

attenuation factor 10, average exposure time ~ 10 s per frame). A few, very strong reflections were still overexposed even when measuring with reduced dose and could therefore not be used in the further steps of data evaluation.

Lattice identification, integration of Bragg reflections and determination of a proper scale factor for merging the datasets were carried out with the program package *XDS* (Kabsch, 1993). To optimize the intensity-to-noise ratio in the merged dataset, only reflections fulfilling the condition $I_{hkl} > 10\sigma(I_{hkl})$ were taken from the second dataset, which was measured using an attenuated X-ray beam. The number of reflections present in both datasets (3296 unique reflections) was sufficiently large for obtaining a reliable scale factor. For further details about experimental conditions and data reduction see Table 1.

The diffraction pattern clearly indicates the Laue symmetry $m\bar{3}m$ (Fig. 1*b*). The strong reflections mark an underlying 1/7 $\times$ 1/7 $\times$ 1/7 basic structure (average structure) with a periodicity of 6.48 Å, which is slightly larger than that for AT-19. Again, the diffraction pattern cannot be uniquely separated into a set of strong main reflections and weak satellites. The diffraction pattern shows no structured diffuse scattering that could be clearly distinguished from background scattering.

2.2.3. ACT-71. The experiment was performed at the synchrotron source SLS, Villigen, Switzerland (beamline X06SA), using a PILATUS 6M pixel detector (Kraft *et al.*, 2009). The energy threshold of the detector was set to discriminate fluorescence scattering from Cu and Ta allowing an accurate measurement of weak reflections. The data were collected on two different crystals from the same batch. A larger crystal was used for measuring the weak intensities (crystal size approximately $20 \times 30 \times 40$ µm^3, 3600 frames, $\Delta\varphi = 0.1^\circ$, exposure time 0.5 s per frame), and a smaller one for the measurement of strong reflections (approximately $5 \times 5 \times 10$ µm^3, 7200 frames, $\Delta\varphi = 0.05^\circ$, exposure time 0.2 s per frame). As a consequence of the very short experimental time (in total about 30 min per run) and because of the stable storage ring current delivered by SLS, primary beam intensity variations could be neglected. As for ACT-45, a few of the strongest reflections could not be measured even when using the smaller crystal. Further details about experimental conditions are shown in Table 1.

Determination of the lattice parameters, integration of Bragg reflections and scaling of the data were carried out using the package *XDS* (Kabsch, 1993) as described above for ACT-45. Again, only reflections with $I_{hkl} > 10\sigma(I_{hkl})$ were taken from the dataset measured for the smaller crystal. The number of reflections present in both datasets was 9148 and therefore large enough to determine a proper scale factor for merging the datasets. The Laue symmetry found was $m\bar{3}m$. However, ACT-71 shows pseudo-extinctions according to a pseudo-*d* glide plane. The reflections violating the extinction rule of the *d* glide plane are of significant intensity (Fig. 2). An experimental effect that could give rise to intensities violating the extinction rules is *Umweganregung* (multiple diffraction). In the case of a randomly oriented crystal, as was the case in our experiments, symmetrically equivalent reflections would cross the Ewald sphere with different scattering vector orientations. Consequently, their intensities would be biased by *Umweganregung* differently, if at all. Since the respective reflections are consistent with the Laue symmetry, however, *Umweganregung* will not play a major role for the violation of the *d* glide plane extinction rule although some contributions cannot be ruled out.

The strong reflections in the full dataset indicate the presence of a 1/11 $\times$ 1/11 $\times$ 1/11 underlying basic periodicity (average structure) of 6.50 Å, which is very similar to the periods observed for the super-lattices in AT-19 and ACT-45 (Fig. 1). Again, the intensities cannot be clearly divided into strong main reflections and weak satellites. Similar to AT-19 and ACT-45 there is no significant structured diffuse scattering in the diffraction pattern (Fig. 1).

2.3. Structure solution and refinement

2.3.1. General procedure. The structures of ACT-45 and ACT-71 were solved using the charge-flipping algorithm, as implemented in the program *SUPERFLIP* (Palatinus & Chapuis, 2007). The input file needed for running *SUPERFLIP* was created by the program *JANA*2006 (Petricek *et al.*, 2006). The optimum flip threshold δ was determined by an automatic procedure implemented in *SUPERFLIP*. After convergence of charge flipping, five cycles using the low-density elimination method (Shiono & Woolfson, 1992) followed to smooth the electron density. The electron-density

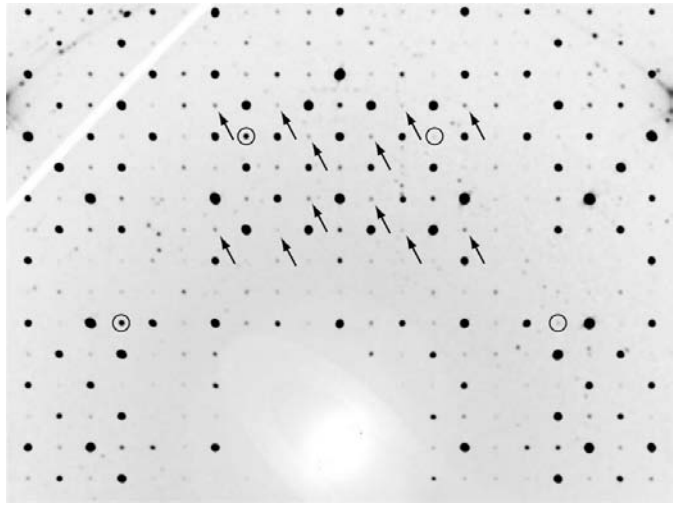

Figure 2
Section from the *hk*0 layer of ACT-71. Some of the reflections violating the extinction rule $h + k = 4n$ and $h, k = 2n$ (n = integer) of the space group $Fd\bar{3}m$ are marked. Some reflections having similar intensities at equivalent positions according to the vertical mirror plane are marked by arrows, while examples of reflections showing strong disagreements are marked by circles. The latter effect might be caused by *Umweganregung*. The pattern ranges from -0.3 to 0.3 Å^{-1} along the horizontal direction and from -0.05 to 0.4 Å^{-1} along the vertical direction. To obtain a better visual impression of the intensities, the pattern was convoluted with a Gaussian with FWHM of 0.00125 Å^{-1}. The off-lattice spots in the pattern may originate from small grains attached to the surface of the crystal, and the white arc in the top left part of the image from the blind areas of the PILATUS 6M detector.

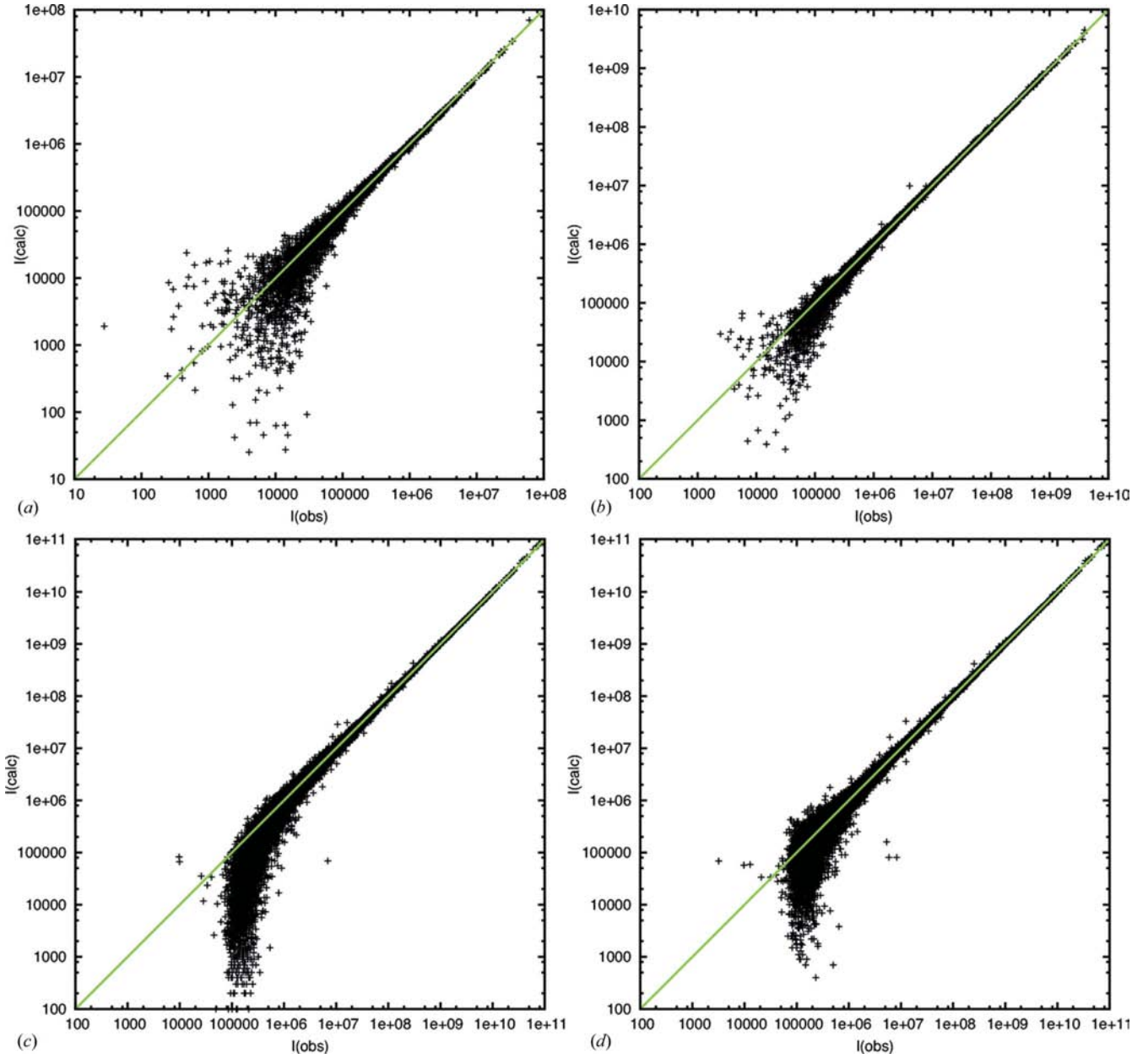

Figure 3
I_{obs} *versus* I_{calc} plots resulting from the refinements of (*a*) AT-19, (*b*) ACT-45 as well as of (*c*) ACT-71 in space group $Fd\bar{3}m$ and (*d*) in $F\bar{4}3m$. The intensities are given in arbitrary units.

maps were interpreted with the program *EDMA* (van Smaalen *et al.*, 2003).

Since charge flipping is a Fourier recycling technique it is very sensitive to missing strong reflections, as is the case for our synchrotron datasets. Therefore, the structures were solved using in-house datasets measured with a standard experimental setup (Oxford Diffraction Onyx CCD diffractometer, resolution 0.67 Å in both cases), which are complete but less accurate than the synchrotron data. The structure model was completed by difference-Fourier techniques and refined against the synchrotron data using the program *SHELXL*97 (Sheldrick, 2008). The initial structure model of AT-19 was taken from Mahne & Harbrecht (1994) and the structure was also refined with *SHELXL*97.

The general strategy for all refinements was as follows. Fully occupied Ta sites were refined with anisotropic displacement parameters (ADPs), while Al and Cu sites as well as split positions were generally refined with isotropic displacement parameters. Al or Cu sites were only anisotropically refined in cases when the refinements gave clear indications for the presence of strongly elongated or disc-like displacements, which could not be described as split positions. Partially or mixed occupied positions were all constrained to one common isotropic Debye–Waller factor in order to avoid correlations

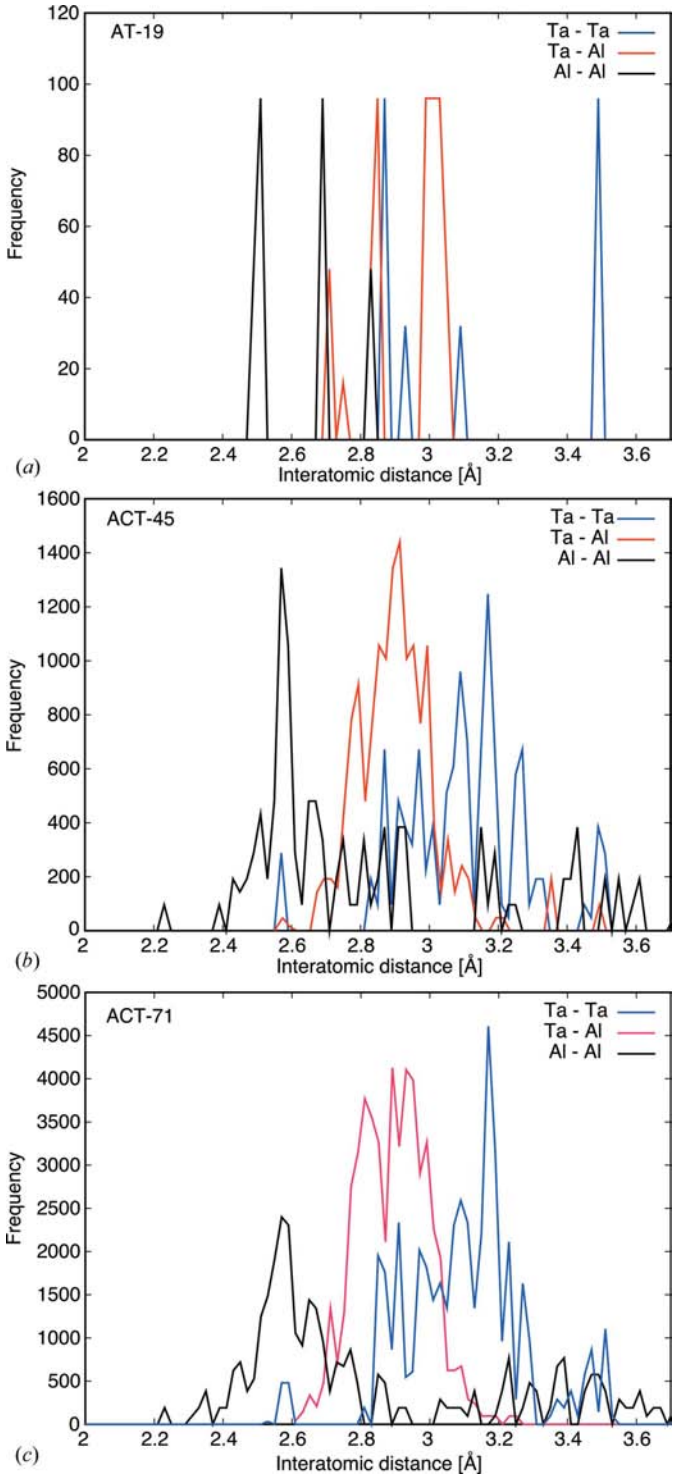

Figure 4
Histograms of next-neighbour atomic distances of the compounds (*a*) AT-19, (*b*) ACT-45 and (*c*) ACT-71. Frequencies are calculated for the atoms within one unit cell and for ordered atoms only. Cu distances in ACT-45 and ACT-71 are therefore not shown as Cu is only found on Al/Cu mixed sites. The bin size of the histograms is 0.02 Å. All next-neighbour distances are within the range of the expected distances apart from a few outliers with very short distances (∼ 2.2 Å for Al—Al and ∼ 2.5 Å for Ta—Ta). Interestingly the short distances are consistently found in ACT-45 and in ACT-71. For a discussion on the short distances see part II of this series.

between displacement parameters and site-occupancy factors. Atoms belonging to the same group of split atoms were constrained to a common isotropic displacement parameter. An atomic site was refined as a mixed Al/Cu site if its scattering power was stronger than Al and weaker than Cu, indicated by too small or too large displacement parameters. The sum of the occupancies of mixed Al/Cu sites was constrained to one, and the relative occupancies were refined. When large ADPs were found for Al atoms the possibilities of split positions or strong anisotropic displacements were considered. If neither possibility seemed likely then the site was refined partially occupied.

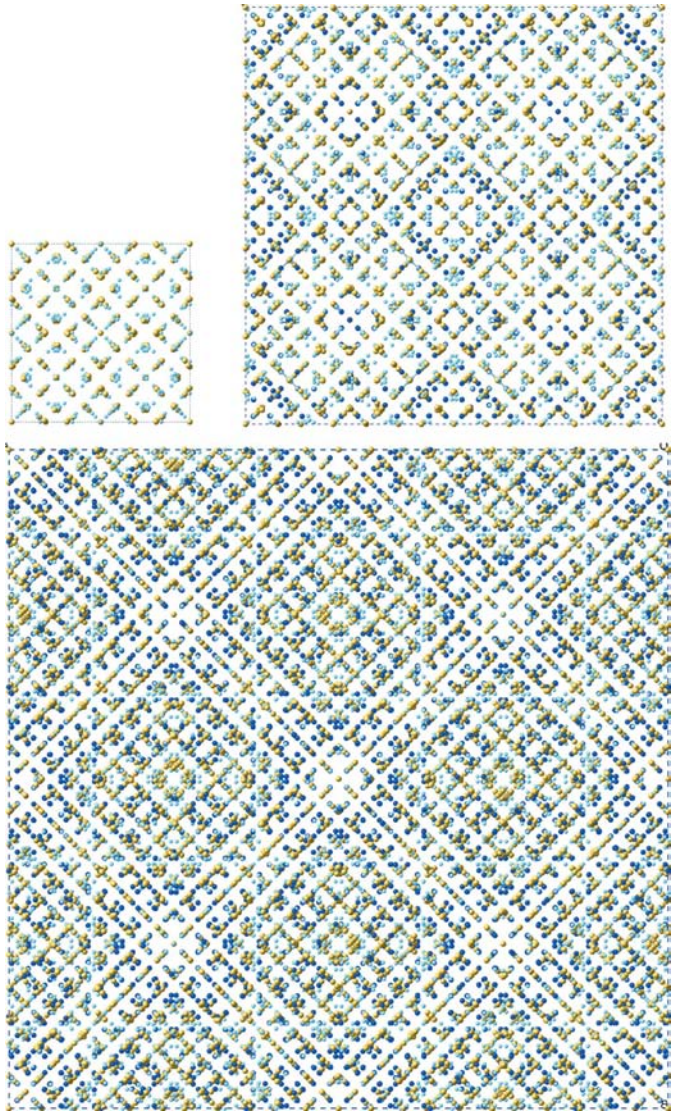

Figure 5
Projections of the unit cells of the structures AT-19, ACT-45 and ACT-71 along a main axis. Ta atoms are shown in brown, Al atoms in light blue and mixed Al/Cu positions in dark blue. Despite the well defined cluster structure, a clear organization into atomic layers containing subcells is obvious, as known from Frank–Kasper phases. However, these subcells are not related to the average structure common to all three phases.

2.3.2. Refinement of AT-19. The major features of the structure reported by Mahne & Harbrecht (1994) could be confirmed; however, some noticeable differences concerning disorder are found. To preserve comparability with the previous refinement we used the same atomic labels. The atoms Al1–5 form an Al76 fullerene cluster, Al6–8 a rhombic dodecahedron, Al9 a cuboctahedron (see Fig. 1 of part II).

The biggest differences between the two refinements are at the aluminium site Al3: the site is split into a major part ($\sim$ 88%) containing Al and a minor part ($\sim$ 12%) containing Ta. The separation is 0.48 Å. The neighbouring Al1 site is split into three positions [ratio of occupancies 0.71 (1):0.144 (5):0.144 (5)], which form a very complicated arrangement when including symmetrically equivalent positions (maximum separation: 1.58 Å).

Both the Al6 and the Al8 sites are now refined as split positions, each due to a shift off a symmetry element (separation of Al6: 0.40 Å and of Al8: 0.44 Å). This is justified by strongly anisotropic ADPs found when refining the atoms on the initial higher symmetry special position, and by a better fit when refining the sites as split positions. In contrast to the results of Mahne & Harbrecht (1994), Al8 is fully and not half occupied. This is important, otherwise there would be too much empty space around the central Ta atom, leading to strong distortions of the coordination polyhedra. Another two atoms form split positions in the vicinity of Al6 and Al8: the tantalum site Ta3 is split into a position occupied by 82% and a second one, bearing the remaining 18% (separation: 0.22 Å). A fraction of 23% of the atoms occupying the Al9 site, a direct neighbour of the Al6 split position, are shifted towards Al6 (separation of Al9: 0.31 Å). The disorder phenomena indicate a small, traceable homogeneity range of AT-19.

The final R values are satisfying (R_1 = 0.060, wR_2 = 0.084, number of parameters/unique reflections: 62/3661)[3] and the refined composition is $Al_{63.6}Ta_{36.4}$. The refinement of the Flack parameter (Flack, 1983) indicated the presence of a $\sim$ 50:50 inversion twin. The I_{obs} *versus* I_{calc} plot, a bond distance histogram and a projection of the structure along a main axis are shown in Figs. 3, 4 and 5, respectively. For further details about the refinement see Table 1.

The large residual difference electron densities, 9.802 e Å^{-3} at a distance of 0.08 Å from Ta5 and $-$10.35 e Å^{-3} found 0.28 Å away from Ta2, most probably result from the high noise level in the high-angle data. When refining the same data with a maximum resolution of d = 0.7 Å, we observed no residuals with absolute values larger than 3.4 e Å^{-3}.

In order to show the electron-density distribution around the split positions of the innermost cluster shell, a rhombic dodecahedron (see Fig. 1*a* of part II), calculations by the method of entropy maximization (MEM) have been performed using the program *BAYMEM* (van Smaalen *et al.*, 2003). Contrary to simple Fourier maps, MEM maps are free of truncation effects (Fig. 6).

[3] Definition of R values: $R_1 = (\sum_i ||F_{i,obs}| - |F_{i,calc}||)/\sum_i |F_{i,obs}|$, $wR_2 = \{[\sum_i w_i(F^2_{i,obs} - F^2_{i,calc})^2]/[\sum_i w_i(F^2_{i,obs})^2]\}^{1/2}$.

2.3.3. Structure solution and refinement of ACT-45. The structure could be solved without any problems as described above. The electron density obtained by charge flipping clearly indicates a non-centrosymmetric space group. All 53 Ta sites and 27 out of 62 Al or mixed Al/Cu sites could be found after a single charge-flipping run. All maxima of the electron-density maps were assigned to the correct chemical element, apart from disordered Ta atoms and from mixed Al/Cu positions. The structure model was completed and refined straightforwardly as described above. After finishing the least-squares refinement, 50 out of 53 Ta sites were found to be ordered, *i.e.* they are fully occupied and show physically reasonable ADPs (all principal mean-square atomic displacements are smaller than 0.012 Å^2). Each of the other three Ta sites is threefold split with total site occupancies 0.5 Ta, 1 Ta, and 0.5 Ta + 0.5 Cu, respectively. In the latter case, Ta and Cu alternately occupy the corners of a pseudo-sixfold ring with a diameter of $\sim$ 0.8 Å; in the other cases, the separations between Ta atoms range from 0.38 to 0.76 Å. All other Cu atoms, apart from that sharing a split position with Ta, are exclusively found mixed with Al, *i.e.* no atomic site is fully occupied with Cu. Altogether 16 mixed Al/Cu sites could be identified. Three of them are almost equally occupied by Cu and Al, while all others host at least more than twice as much Al than Cu. There are 45

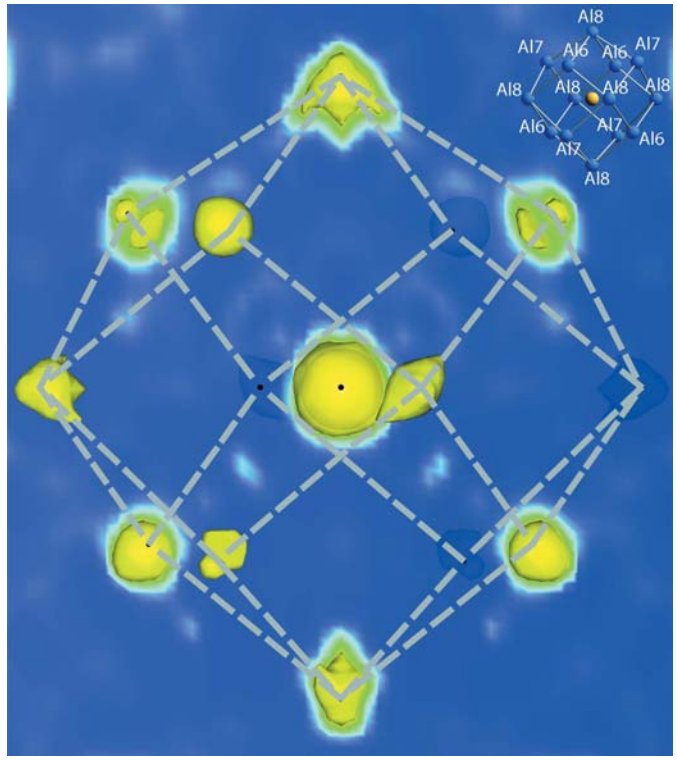

Figure 6
Electron-density distribution around the positions of Al6–8, as calculated by MEM based on a very large X-ray diffraction dataset. One sees that the triple-split position of Al7 is even a tetrahedral one, and the double-split position of Al8 a triangular one. The underlying rhombic dodecahedron, which is the innermost shell of the fullerene cluster, is drawn (see also Fig. 1*a* of part II). The high density in the centre is caused by a Ta atom. For clarity, electron densities in the back of the rhombic dodecahedron are shown as blue shadows only.

Al sites without any refineable Cu contributions; 34 of them show no indication of significant disorder, seven exhibit significant ADPs (maximum principal mean-square displacements range between 0.034 and 0.0995 Å^2) and four Al sites are split with distances between 0.56 and 0.97 Å. Refinement of the Flack parameter indicates the presence of an inversion twin. The twin ratio found for this sample is 0.376 (5):0.624 (5).

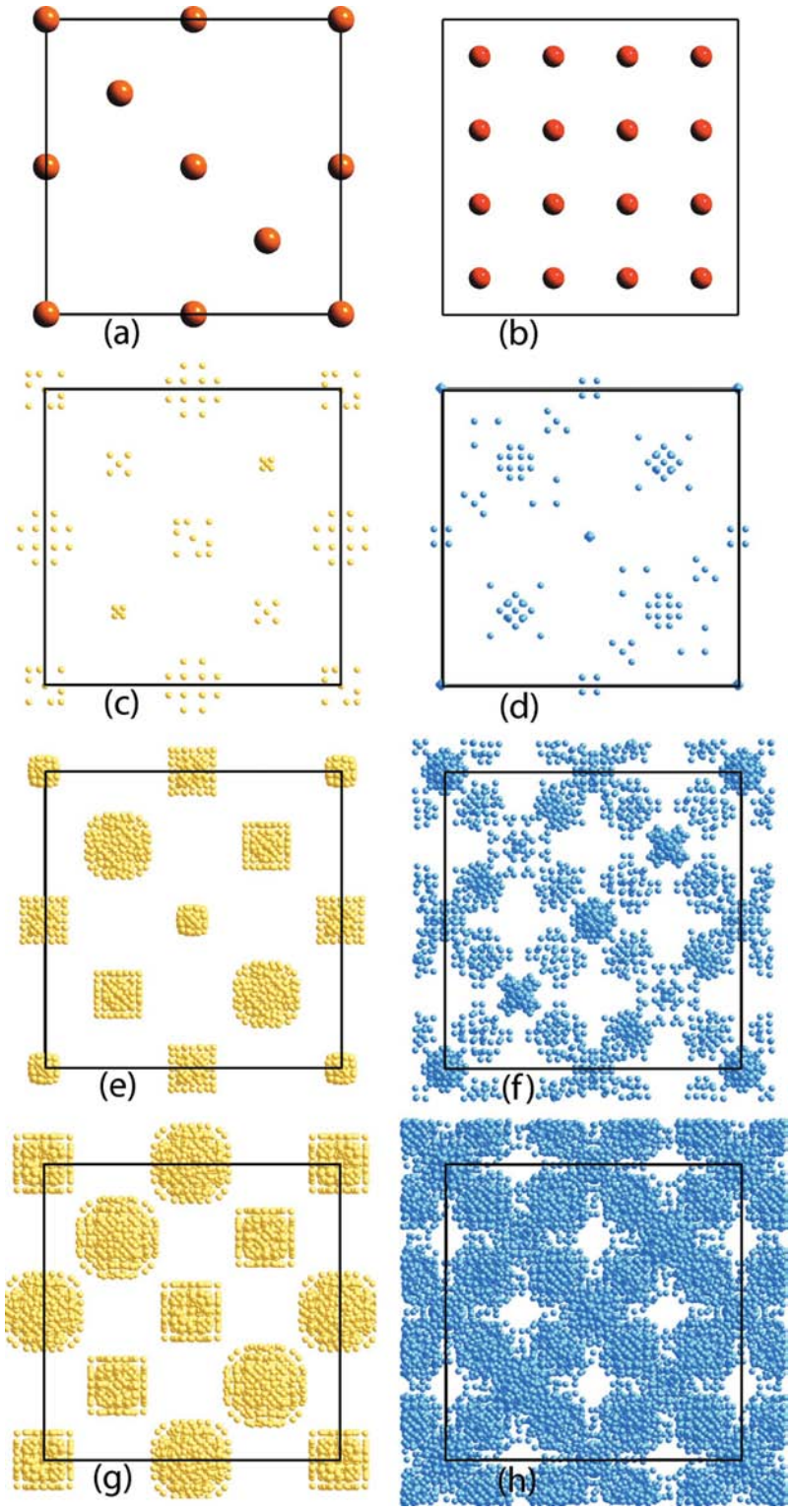

Figure 7
(*a*) Mg and (*b*) Cu partial structures of the cubic Laves phase *cF*24-$MgCu_2$. Average structures of (*c*)–(*d*) AT-19 (a = 6.384 Å), (*e*)–(*f*) ACT-45 (a = 6.495 Å) and ACT-71 (a = 6.499 Å). The Ta partial structures are depicted in (*c*), (*e*) and (*g*), those of Al in (*d*), (*f*) and (*h*). In all cases, projections along [001] of half a unit cell are shown.

Fig. 3 shows the I_{obs} *versus* I_{calc} scatterplot, which clearly reflects the high quality of the refinement. Apart from a few outliers, the calculated intensities are very close to the experimental values, even for the weak reflections. There is a small bias towards too large observations in the case of small intensities, what might result from a systematic integration of background scattering during data reduction, minor shortcomings of the model or moderate contributions of *Umweganregung*.

The final R values are satisfying (R_1 = 0.019, wR_2 = 0.0459, number of parameters/unique reflections: 520/11 816) and the refined composition is $Al_{56.6}Cu_{3.9}Ta_{39.5}$, which is in fair agreement with the composition $Al_{53.4}Cu_{6.3}Ta_{40.3}$, as obtained by EDX. The small deviations found for Al and Cu concentrations may be explained by inaccuracies in the EDX measurement and by the restriction that all mixed positions are constrained to a common ADP, which certainly biases the refined occupancies. Next-neighbour bond distances are shown in Fig. 4 and a projection of the structure along a main axis is given in Fig. 5.

2.3.4. Refinement of ACT-71. The structure was solved in the same way as reported for ACT-45. Owing to the strong pseudo-symmetry, *SUPERFLIP* suggested the centrosymmetric space group $Fd\bar{3}m$. As the symmetry is only weakly broken, we started structure refinement in this space group. The interpretation of the electron density gave even more satisfying results than was the case for ACT-45. All 77 Ta sites and 88 out of 106 Cu or Al sites finally found after refinement in the space group $Fd\bar{3}m$ could be identified after one charge-flipping run. All electron maxima were assigned to the correct chemical element apart from Ta split sites and from the obvious ambiguity at mixed Al/Cu positions. Again, the structure model could be easily completed using the difference-Fourier method. Then, the structure was refined in a similar way as described above. The final R values for the refinement in $Fd\bar{3}m$ were R_1 = 0.0346 and wR_2 = 0.0924 (number of parameters/unique reflections: 865/24 117). Despite the low R values, the refinement was not satisfying since the reflections violating the *d*-glide plane extinction rule were neglected. Furthermore, weak intensities could not be fitted sufficiently. As can be seen in the I_{obs} *versus* I_{calc} plot (Fig. 3),

there is a clear tendency for weak reflections to be observed as stronger than they are calculated. This can hardly be explained by experimental artefacts like *Umweganregung* or integration of background scattering during data processing; it is just a consequence of the wrong space group, as will be shown below.

When dropping the *d* glide plane, as needed due to the violation of the extinction rule, three subgroups with cubic symmetry may be chosen: $F\bar{4}3m$, $F4_132$ and $F23$, which is a common subgroup of $F\bar{4}3m$ and $F4_132$. Since the fourfold symmetry is clearly obeyed and the extinction rule for a 4_1 screw axis is not observed, only $F\bar{4}3m$ is left, the same space group as found for AT-19 and ACT-45. The structure model was extended to this non-centrosymmetric space group by applying inversion symmetry to the atoms of the asymmetric unit for $Fd\bar{3}m$. Correlations due to the strong pseudo-symmetry did not allow a fully independent refinement of the atoms that are related by the pseudo-inversion symmetry. Therefore, the ADPs of these atoms had to be constrained. No other constraints were applied beside those mentioned in the description of the general strategy.

154 symmetry-independent Ta sites were refined in $F\bar{4}3m$; 150 of them are fully occupied and all principal mean-square atomic displacements are smaller than 0.014 Å^2. The remaining four Ta atoms occupy threefold split positions with interatomic separations between 0.43 and 1.05 Å. The distribution of Cu is similar to ACT-45, *i.e.* all Cu atoms are mixed with Al. Altogether 73 sites mixed occupied by Al/Cu could be identified, of which only seven contain more Cu than Al. The maximum occupancy of Cu on a single site is 0.73. There is no Ta/Cu split position, as observed for ACT-45. 136 Al sites are without any detectable Cu contribution; 18 of them show strongly anisotropic ADPs (maximum principal mean-square displacements range from 0.052 to 0.1158 Å^2) and seven are not fully occupied (occupation factors between 0.553 and 0.802). The *R* values of the refinement in $F\bar{4}3m$ are considerably smaller than those for the refinement in $Fd\bar{3}m$ (R_1 = 0.0237 and wR_2 = 0.0611, number of parameters/unique reflections: 1393/48 023). The calculated composition $Al_{55.4}Cu_{5.4}Ta_{39.2}$ is close to the nominal composition $Al_{55}Cu_5Ta_{40}$.

The I_{obs} *versus* I_{calc} plot is now much more symmetric than for the refinement in the centrosymmetric space group $Fd\bar{3}m$ (Fig. 3*d*). Nevertheless, there is still a tendency for weak reflections to be stronger as observed than as calculated. In particular, a striking, almost sharp, lower limit for observed intensities can be identified. The origin of this behaviour is not clear. *Umweganregung* or deficits in the model would not lead to such a sharply defined effect. More likely this results from an artefact during data processing, *e.g.* due to an improper handling of background scattering. So far there is only a little experience regarding the combination of the PILATUS 6M detector with the program *XDS* for processing diffraction patterns from inorganic crystals with a low background and a high dynamic range of intensities (Weber *et al.*, 2008). Because of missing reference experiments, the question of the origin of the asymmetry in the I_{obs}/I_{calc} plots at very low intensities must be left open.

Refinement of the Flack parameter indicated the presence of an approximately 50:50 inversion twin. The Flack parameter was also refined against unmerged data, in order to be sure that the observed twinning is not an artefact from merging two datasets from untwinned crystals. The refinements converged to approximately the same value as obtained with merged data. Next-neighbour bond-distance histograms are shown in Fig. 4 and a projection of the structure along a main axis is seen in Fig. 5.

2.3.5. Distance distributions and average structures. The distribution of atomic distances is similar in all three cases, AT-19, ACT-45 and ACT-71 (Fig. 4). The main difference is that the peaks are narrow and well separated for AT-19, while they appear considerably broadened in the cases ACT-45 and ACT-71. It appears that the number of shorter distances grows at the cost of longer ones with increasing unit-cell size. Additionally, very short Ta—Ta distances of 2.536 Å and a few Al—Al distances between 2.2 and 2.4 Å show up for both ACT-45 and ACT-71. The short Ta—Ta distance is caused by covalent bonding as we will show in part II. The short Al—Al distances are found in environments with several split positions and might be artefacts.

Some information about the relationships between the structures of AT-19, ACT-45 and ACT-71 can be obtained from the projections of the structures (Fig. 5). Although the structures appear to be mainly organized in layers, some features of clusters can be identified as well. These features are typical for the tetrahedrally close-packed Frank–Kasper phases (Frank & Kasper, 1958, 1959). There is also some similarity to the projected structure of a fictitious cubic Laves phase *cF*24-Ta(Al,Cu)$_2$. The lattice parameters of the Laves phase and of AT-19, ACT-45 and ACT-71 are in the ratio 1:3:7:11, if we assume a lattice parameter of $a \simeq 6.5$ Å for Ta(Al,Cu)$_2$. This ratio is reflected in the indices of the strongest Bragg reflections, which are 220 for Ta(Al,Cu)$_2$, 660 for AT-19, 14,14,0 for ACT-45, and 22,22,0 for ACT-71, indicating the existence of a common average structure for all three phases (Fig. 7). AT-19, ACT-45 and ACT-71 are $3 \times 3 \times 3$, $7 \times 7 \times 7$ and $11 \times 11 \times 11$ superstructures of this average structure. Its space group is $F\bar{4}3m$, averaged Ta occupies Wyckoff positions 4*a*–*d*, and averaged Al Wyckoff position 16*e* *x* *x* *x*, with *x* = 1/8, 3/8, 5/8 and 7/8. If occupied by real atoms, all positions would have to be half-occupied due to otherwise too short distances.

It is amazing that such complex cluster structures of quite different unit-cell dimensions have the same simple and well defined average structure. We found similar simple average structures for other structures with giant unit cells such as the Samson phase *cF*1168-Mg_2Al_3 (Feuerbacher *et al.* 2007) and *cF*488-$Li_{13}Na_{29}Ba_{19}$ (Smetana *et al.*, 2006).

The existence of a common average structure helps one to understand the formation of such complex structures. The actual structures with giant unit cells appear as ordered variants of the underlying simple structure, which is related to the cubic Laves phase. At least two competing local ordering

parameters are responsible for the formation of the giant unit cells with only particular superstructure periods. One leads to the formation of clusters, the other is the formation of as large as possible fragments of the Laves phase. Another consequence is the existence of densely occupied and densely packed puckered netplanes, *i.e.* thick atomic layers. For instance, in the case of ACT-71, symmetrically equivalent (111) netplanes would have a distance of 41.275 Å compared with 3.752 Å in the average structure. The puckering of the atomic layers would be within approximately ±1.4 Å.

Based on the close similarity of the average structures, it is worthwhile to study whether they can be seen as commensurate lock-in structures of a common incommensurately modulated structure. This approach has been successfully applied for the classification of several structure families, albeit much simpler ones (see, for instance, Elcoro *et al.*, 2008, and references therein). A more detailed quantitative study will be part of future work.

3. Conclusions

ACT-71 is the intermetallic phase with by far the largest unit cell known so far. Despite the complexity of its structure (*e.g.* an unusually large number of atoms per unit cell, significant disorder, large absorption coefficients and the presence of pseudo-symmetry), the charge-flipping algorithm allowed structure solution without major problems even when using in-house data. Owing to the high quality of the synchrotron data and the properties of the PILATUS 6M detector, it was possible to refine the structure to a degree of accuracy and reliability that is quite unusual for such complex intermetallics. The low R values and physically reasonable results regarding bond lengths, refined composition and ADPs, justify the constraints applied and emphasize the quality of the experimental data as well as the reliability of the structure refinements.

It is surprising that no significant diffuse scattering could be observed even when using the PILATUS 6M detector, which was demonstrated to belong to the most efficient instruments when measuring weak diffraction signals (Weber *et al.*, 2008). This can be understood when considering that most disorder is found on the weakly scattering Al or Cu sites. Furthermore, if disorder does not show any long-ranging spatial correlations, resulting diffuse scattering is very broad and can hardly be distinguished from parasitic background scattering.

Ambiguities in the determination of the space group of ACT-71 could be finally resolved by showing that the weak reflections violating the extinction rule of the d glide plane are most probably not dominated by *Umweganregung*. Further, considerably better R values and a significantly better agreement in the I_{obs} *versus* I_{calc} plots support the assumption that the true space group of ACT-71 is $F\bar{4}3m$, even though the difference from the structure obtained with $Fd\bar{3}m$ is small.

The reinvestigation of AT-19, confirmed in general the findings by Mahne & Harbrecht (1994). Our high-resolution dataset, however, allowed a more precise and reliable description of structural details in agreement with quantum-mechanical calculations (see part II). Contrary to the previously published structure we found for the crystal we studied that all sites are fully occupied, but six out of 17 atomic positions are split. Some of the distances between split positions are very short, but the high-resolution measurement clearly allowed us to distinguish split positions from anisotropic displacements.

The identification of a common basic periodicity of *ca* 6.5 Å for all three compounds studied in this work may stimulate a description of these and other complex crystal structures as cluster-driven superordering of fundamental structures such as Laves phases. A detailed description of the cluster-based structures will follow in part II of this paper.

We acknowledge support by the staff of the Swiss–Norwegian beamline (SNBL) at ESRF and the protein crystallography beamline X06SA at the SLS.

References

Černý, R., François, M., Yvon, K., Jaccard, D., Walker, E., Petříček, V., Císařová, I., Nissen, H.-U. & Wessicken, R. (1996). *J. Phys. Condens. Matter*, **8**, 4485–4493.
Conrad, M. & Harbrecht, B. (2007). *Philos. Mag. Lett.* **87**, 493–503.
Conrad, M., Harbrecht, B., Weber, T., Jung, D. Y. & Steurer, W. (2009). *Acta Cryst.* B**65**, 318–325.
Elcoro, L., Perez-Mato, J. M., Friese, K., Petříček, V., Balić-Žunić, T. & Olsen, L. A. (2008). *Acta Cryst.* B**64**, 684–701.
Feuerbacher, M. *et al.* (2007). *Z. Kristallogr.* **222**, 259–288.
Flack, H. D. (1983). *Acta Cryst.* A**39**, 876–881.
Frank, F. C. & Kasper, J. S. (1958). *Acta Cryst.* **11**, 184–190.
Frank, F. C. & Kasper, J. S. (1959). *Acta Cryst.* **12**, 483–499.
Fredrickson, D. C., Lee, S. & Hoffmann, R. (2007). *Angew. Chem. Int. Ed.* **46**, 1958–1976.
Kabsch, W. (1993). *J. Appl. Cryst.* **26**, 795–800.
Kraft, P., Henrich, B., Eikenberry, E. F. & Broennimann, C. (2009). *J. Synchrotron Rad.* **16**, 368–375.
Mahne, S. & Harbrecht, B. (1994). *J. Alloys Comput.* **203**, 271–279.
Nowotny, H. & Österreicher, H. (1964). *Monatsh. Chem.* **95**, 982–989.
Oxford Diffraction (2008). *CrysAlis CCD* and *CrysAlis RED*, Version 1.171.32.24. Oxford Diffraction Ltd, Abingdon, Oxfordshire, England.
Palatinus, L. & Chapuis, G. (2007). *J. Appl. Cryst.* **40**, 786–790.
Petricek, V., Dusek, M. & Palatinus, L. (2006). *JANA*2006. Institute of Physics, Prague, Czech Republic.
Sheldrick, G. M. (2008). *Acta Cryst.* A**64**, 112–122.
Shiono, M. & Woolfson, M. M. (1992). *Acta Cryst.* A**48**, 451–456.
Smaalen, S. van, Palatinus, L. & Schneider, M. (2003). *Acta Cryst.* A**59**, 459–469.
Smetana, V., Babizhetskyy, V., Vajenine, G. & Simon, A. (2006). *Angew. Chem. Int. Ed.* **45**, 6051–6053.
Stein, F., Palm, M. & Sauthoff, G. (2004). *Intermetallics*, **12**, 713–720.
Stein, F., Palm, M. & Sauthoff, G. (2005). *Intermetallics*, **13**, 1056–1074.
Weber, T., Deloudi, S., Kobas, M., Yokoyama, Y., Inoue, A. & Steurer, W. (2008). *J. Appl. Cryst.* **41**, 669–674.